

Elastic waves above elastically driven instability in weakly perturbed channel flow

Ron Shnapp¹ and Victor Steinberg^{1,2}

¹*Department of Physics of Complex Systems, Weizmann Institute of Science, Rehovot 76100, Israel*
²*The Racah Institute of Physics, Hebrew University of Jerusalem, Jerusalem 91904, Israel*

This letter presents experimental results and reveals that strong perturbations are not necessary for elastic instability to occur in straight channel visco-elastic flows. Our analysis shows that a non-normal mode bifurcation is followed by elastic waves on top of chaotic fluctuations at higher frequencies. This persists in the transition, elastic turbulence, and drag reduction regimes with a non-monotonic variation of the intensity. Furthermore, our measurements allow us to obtain the dependence of the wave velocity on Wi and confirm their linear dispersion for the first time directly.

The laminar flow of a viscous solvent is strongly modified by adding a tiny amount of long polymer molecules, resulting in elastically driven instability, and further, in a state of chaotic flow called elastic turbulence (ET). ET occurs at the Reynolds number $Re \equiv UL\rho/\eta \ll 1$ and the Weissenberg number $Wi \equiv U/L\lambda > 1$, where U , L , ρ , and η are the characteristic velocity and length scales, the fluid's density and viscosity respectively, and λ is the polymer relaxation time; Wi is a control parameter that defines the degree of polymer stretching by the flow [1]. Until recently, the elastically driven instabilities and ET were predicted and observed only in various flow geometries with curvilinear streamlines, whereas they vanish in the limit of zero curvature [1–5]. The problem we address in this study concerns the emergence of instabilities in a straight channel flow of visco-elastic fluid at $Re \ll 1$ and $Wi \gg 1$ without prearranged perturbations. Even though a linear stability analysis of elastically driven parallel shear flows (plane Poiseuille and plane Couette flows) predicts their absolute linear stability at all Wi [2], theoretical developments [6–10] suggest two different mechanisms of possible elastically driven instability in these flows. Moreover, experiments in straight pipe and square channel flows with strong prearranged perturbations at the inlet [11–14] reveal that large velocity fluctuations develop downstream from the inlet, which suggests the appearance of an elastic instability.

In recent work, we reported experimental studies of elastic instability and associated flow structures in a straight quasi-2D channel flow of visco-elastic fluid with strong prearranged perturbations at the inlet [15]. There, three flow regimes were observed above the instability onset: transition, ET, and drag reduction (DR). Our measurements of flow friction, pressure, and velocity fluctuations in the streamwise and spanwise directions, indicate that the transition at $Re \ll 1$ and $Wi \gg 1$ is continuous and non-hysteretic. Notably, this case is different from the classical continuous linear transition via the most unstable linear normal mode [16]. In the latter, the normalized friction factor, C_f/C_f^{lam} grows above the transition onset as a power-law $(Wi - Wi_c)^{0.5}$, and in the case of the Hopf bifurcation, a corresponding os-

cillation frequency of a single stable mode varies linearly with $Wi - Wi_c$ (here, Wi_c is the critical value at the onset). In contrast to that, in the experiment discussed, C_f/C_f^{lam} grows algebraically as $Wi^{0.125}$, the frequency of the elastic waves varies non-linearly with $Wi - Wi_c$ above the onset, and the velocity power spectrum is continuous with a high frequency decay exponent of about -1.7 . These observations imply a random flow with an elastic wave peak at low frequencies on top of it [15], and they indicate that the found elastic instability is not the classical linear one via the most unstable, exponentially growing, single normal mode, but it is associated with a transition due to non-normal modes [17]. Moreover, the most striking finding is the discovery of weakly unstable coherent structures (CSs) in the form of streamwise rolls and streaks, self-organized into a cycling self-sustained process (SSP) [15]. The former generates the latter via an elastic analogy of a lift-up mechanism suggested in Ref. [9, 10], similar to that first described in Newtonian parallel shear flows [18]. In ET, the streaks are destroyed by a secondary elastically driven interface instability, which has a remarkable visual resemblance to the inertially driven Kelvin-Helmholtz instability [19]. The sequence of CSs repeats periodically due to elastic waves that pump energy into the cycle [15]. This characteristic of ET distinguishes it from inertial turbulence in parallel shear flows. In light of the above findings, several questions arise regarding the role of perturbations in the development of elastic instabilities. (i) Are the strong prearranged perturbations necessary for the elastic instability in a straight channel flow of visco-elastic fluid? (ii) If it is not, will very weak but finite-size perturbations excite an elastic instability, and, if so, will it be due to normal or non-normal modes? (iii) Will the same or different CSs be selected, if at all? (iv) Which flow regimes above the instability onset will occur? And (v) will the waves and their energizing role persist in such weakly perturbed flows?

In this letter, we present experimental results in visco-elastic channel shear flow with a smoothed inlet and without prearranged strong perturbations. Based on pressure and velocity fluctuations measurements, we found that a small cavity in the top channel wall produces small but

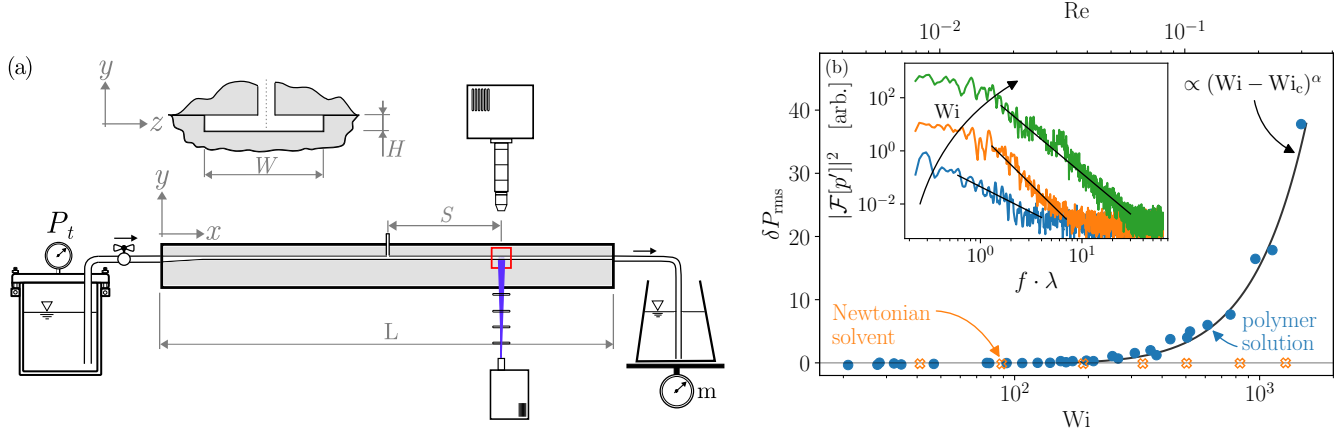


FIG. 1. (a) Schematics of the channel flow apparatus and the PIV system used in the experiments, along with a cross-section view at the center of the channel showing the cavity of diameter $d=H$. The channel dimensions are length (L)x width(W)x height(H)= $750\times3.5\times0.5$ mm 3 . (b) RMS of pressure fluctuations, normalized by experimental noise measured at the cavity location. A fit of the data (black line) gives $\delta P_{\text{rms}} \propto (Wi - Wi_c)^\alpha$ with $Wi_c = 125 \pm 25$ and $\alpha = 1.85 \pm 0.05$. The inset shows pressure power spectra at $Wi = 32, 520$, and 1478 .

finite-size perturbations that can excite the elastic instability at $Wi > Wi_c \approx 125$. Accordingly, both the pressure and the velocity power spectra are continuous with power-law decays at higher frequencies. Furthermore, we detect the emergence of elastic waves at low frequency, propagating in the span-wise direction. These waves also persisted in ET and DR with a growing intensity of chaotic continuous spectra. Lastly, we measured the dependence of the wave frequency, wavelength, and velocity on Wi independently and confirmed their linear dispersion relation.

The experiment was conducted in a transparent acrylic rectangular channel as shown in Fig. 1a. The fluid was driven by Nitrogen gas pressurized up to 60 psi. The channel inlet is smoothed and tapered to reduce unwanted disturbances to the flow. As a working fluid, we used an aqueous polymer solution comprised of 44% Sucrose, 22% D-Sorbitol, 1% Sodium Chloride (*Sigma Aldrich*), and Polyacrylamide (PAAm, $M_w = 18 \times 10^6$ Da, (*Polysciences inc*) at concentration $c = 230$ ppm with $c/c^* \simeq 1$, where c^* is the overlap polymer concentration [20]. The solution properties, $\rho = 1320$ Kg m $^{-3}$, $\eta_s = 0.093$ [Pas], and $\eta = \eta_p + \eta_s = 0.125$ [Pas] are the solution density, the solvent's and the total solution's viscosity, respectively. The longest polymer solution relaxation time is $\lambda = 12.1$ [s] based on the results of [20]. To get the average velocity $U = \Delta m / (\rho H W)$ we used a PC-interfaced balance (BPS-1000-C2-V2, MRC) to measure the fluid discharge mass $m(t)$ providing the flow discharge rate $\Delta m / \Delta t$ average over Δt . Then, experiments were conducted in the range $Re = \frac{\rho U H}{\eta} < 0.3$ and $Wi = \frac{U}{H} \lambda \in (100, 1700)$, thus in the high elasticity number regime $El = \frac{Wi}{Re} \approx 4500$.

We conducted two separate experiments. First, we

measured the velocity field at various distances, S , downstream from the cavity using particle image velocimetry (PIV) with the end of the cavity blocked; the cavity thus served as a source of weak perturbation (see Fig. 1a). We used a thin laser sheet (thickness of $\sim 30\mu\text{m}$) over the central plane at $y = 0$ to illuminate $3.2\mu\text{m}$ fluorescent particles added to the fluid. The region of interest was imaged by a high spatial resolution 1.280x1.024 Mpx camera (Photron FASTCAM Mini UX100) in the range of 125-4000 fps depending on the flow rate. The OpenPIV software [21] was then used to calculate the 2D velocity components $u_x(t, x, z)$, $u_z(t, x, z)$ in the (x, z) horizontal plane. Second, we measured pressure fluctuations by connecting a pressure sensor to the end of the cavity. We thus measured pressure fluctuations using high-resolution pressure sensors with an accuracy of 0.1% of full scale (Honeywell, HSC Series). We typically conducted long recording sessions, $\sim \mathcal{O}(10)$ minutes or $\sim \mathcal{O}(50\lambda)$ long, for each Wi to obtain sufficient statistics.

In order to characterize the elastic driven instability caused by the small perturbation from the cavity, we calculate the normalized pressure fluctuations, $\delta P_{\text{rms}} = P_{\text{rms}} / P_{\text{rms, lam}} - 1$, as a function of Wi . As shown in Fig. 1b, for sufficiently high Wi it grows as $\delta P_{\text{rms}} \sim (Wi - Wi_c)^{1.85 \pm 0.05}$ with $Wi_c = 125 \pm 25$. In the inset of Fig. 1b, we also show pressure power spectra for three Wi values: below, above, and at Wi very high above the transition. For all cases there are continuous spectra with power-law decays which have exponents of roughly -1.9, -3.75 and -3.2 that indicate three flow regimes.

We further characterize the elastic instability through flow velocity fluctuations using the PIV results. The main panel of Fig. 2a presents the normalized streamwise velocity fluctuations $\delta u_{\text{rms}} = u_{\text{rms}} / u_{\text{rms, lam}} - 1$ ver-

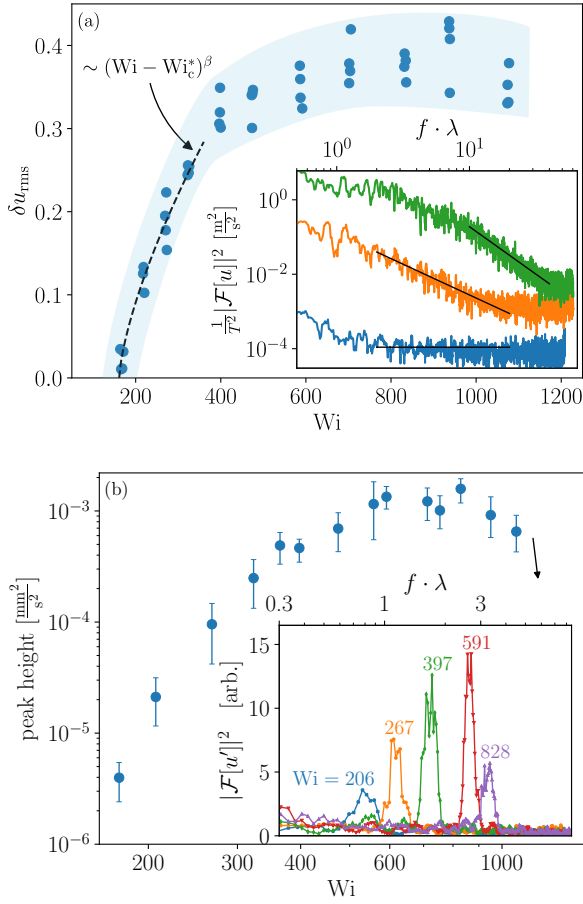


FIG. 2. (a) The normalized RMS of streamwise velocity fluctuations at $S = 170H$. Inset: normalized velocity power spectra in log-log scales at distance $S = 40H$ from the cavity for $Wi = 271, 637$, and 2048 . (b) Height of spectral peaks versus Wi in log-log scales. Inset: Streamwise velocity power spectra at distance $170H$ downstream from the cavity at $z = \pm \frac{1}{6}H$ for 5 Wi values in lin-log scale. The spectra and frequencies are normalized by the noise level and λ , respectively.

sus Wi at the distance $S/H = 170$ downstream from the cavity. For sufficiently high Wi the velocity fluctuations grow as $\delta u_{\text{rms}} \sim (Wi - Wi_c)^\beta$ with $Wi_c = 125 \pm 40$ and $\beta = 0.7 \pm 0.1$. In the inset of Fig. 2a, we show the frequency power spectra of the streamwise velocity component taken closer to the cavity at $S/H = 40$ for three Wi values. The spectra are continuous; for the lowest Wi the spectrum is flat, while for the two higher Wi cases the spectra show algebraic decay with exponents of roughly -1.7 and -2.5 as shown in black lines. The changing slopes indicate the existence of three flow regimes downstream from the cavity.

In addition to the continuous spectra, and farther downstream from the cavity, at $S/H = 170$, we detected peaks of coherent oscillations in the streamwise velocity at $Wi > Wi_c$. These spectral peaks are shown normalized in the inset of Fig. 2b for five Wi values in log-linear

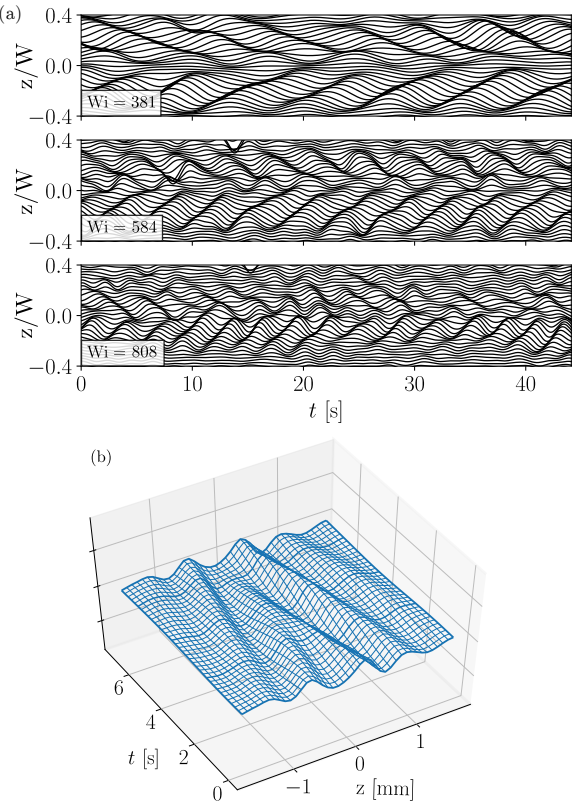


FIG. 3. (a) Space-time plots at $-0.4 < \frac{z}{W} < 0.4$ of the streamwise velocity fluctuations, $u'_x(z, t)$ exhibiting elastic wave structures for three values of Wi . The time series are filtered via a band-pass Butterworth filter centered around the spectral peaks to remove background noise. (b) Streamwise velocity, phase averaged at the elastic wave frequency for $Wi = 407$.

scales. The normalized intensity of the peaks grows for the first four Wi from 206 up to 591 , followed by its sharp reduction at $Wi = 828$, while for higher Wi the peaks became broader and less coherent (not shown). The spectral peak intensity is shown in more detail in the main panel of Fig. 2b and in units of energy per unit mass versus Wi from about 180 up to 1100 in log-log scales. The peak intensity initially increases rapidly with Wi for $180 \lesssim Wi \lesssim 360$; then its growth slows down in the range $360 \lesssim Wi \lesssim 850$ with a consequent saturation and a drop-down to zero at $Wi \geq 1100$. Furthermore, the peak frequency grows with Wi from $f\lambda \approx 0.7$ to roughly 3.5 . The intensity behavior agrees well with our earlier observations in the flow between two obstacles, past an obstacle hindering a channel flow, and, particularly, in a straight channel flow with strong perturbations at the inlet [15, 22]. Moreover, in those flow geometries, the dependence of the wave peak value on Wi correlates with the dependence of the friction factor on Wi exhibiting the transition, ET, and DR regimes [15].

To examine the spatial structure of the velocity field,

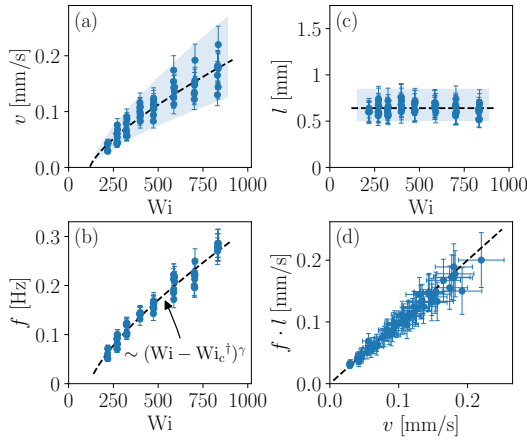


FIG. 4. (a), (b) and (c) show the wave velocity, frequency, and wavelength dependence on Wi , respectively. Dashed lines are the best fits. (d) shows the wave velocity versus $f \cdot l$ that confirms the linear dispersion relation shown as a dashed line.

we plot the streamwise velocity fluctuations, band-pass filtered around the spectral peak frequency, as a space-time plot in Fig. 3a. The structure can be presented more explicitly by phase averaging the velocity fluctuation signals as shown in Fig. 3b for $Wi = 407$. The plots in Fig. 1 reveal a wavy structure of the velocity fluctuations that can be represented very well by the expression

$$u'_x(t, z) = A \exp 2\pi i(f t + l^{-1}|z|) , \quad (1)$$

where A is an amplitude, f is the frequency, and l is a wavelength. Thus, the wavy shape seen in the figure corresponds to wave crests and troughs that travel in the span-wise, z , direction. Furthermore, the angle between the wave crests and the horizontal direction in Fig. 3a corresponds to the wave velocity, v . Thus, from the angle changes with Wi , seen in Fig. 3a, one can estimate the dependence of v on Wi .

In Fig. 4a, b, and c, we plot the three main wave characteristics, f , l , and v , as functions of Wi . The data reveals that l did not depend on Wi in the range explored in the experiments, though it randomly fluctuated in the range $l \in [0.5, 0.8] \text{ mm} \approx [0.14W, 0.22W]$. Thus, it seems that l was determined in our experiment by the channel geometry. On the other hand, f is seen to grow with Wi in Fig. 2b; its Wi dependence can be fitted by a power-law $f \sim (Wi - Wi_c)^\gamma$ with $Wi_c = 119 \pm 30$ and $\gamma = 0.73 \pm 0.05$, shown as a dashed line. Furthermore, in Fig 4d we plot our measurements of v versus $f \cdot l$ and show that, to experimental uncertainty, $v = f \cdot l$, thus confirming the existence of the linear dispersion for the waves in our channel flow. Lastly, despite the data scatter that results from the fluctuations of l , the wave velocity can be fitted with the power law $v \sim (Wi - Wi_c)^\gamma$ that is shown in Fig. 4a as a dashed line, which agrees well with our data trend. Similar power-law exponents for v were

observed in previous measurements of elastic waves by Refs. [15, 22].

Lastly, two types of transverse, linearly dispersed waves are predicted to occur in visco-elastic fluid flows. The first are the shear waves, reviewed in detail in the classical book [23]. The velocity of shear waves is determined by the fluid's elastic shear modulus, similar to solids, so for viscoelastic fluids with sufficiently large relaxation time, the elastic modulus is replaced by the storage modulus $G = \eta/\lambda$ that leads to $v_{sw} = (\eta/\lambda\rho)^{1/2}$. Moreover, shear waves are predicted to appear in visco-elastic flows at the elastic Mach number $M = U/v_{sw} > 1$. The second type of waves, called elastic waves, are analogous to the magneto-hydrodynamic Alfvén waves [22, 24–26]. The velocity of elastic waves depends on the elastic stress in the flow, $v_{el} = (\sigma/\rho)^{1/2}$, and it changes with Wi ; this is in sharp contrast to the shear waves, the velocity of which depends on the fluid properties being constant for each fluid and independent of the flow. Since in our experiment v changed with Wi , we conclude that we observe the elastic waves, as predicted in Refs. [24, 25]. Moreover, the smallest value of $v = 0.03 \text{ mm/s}$ measured in the experiment at $Wi \approx 220$ that corresponds to $U \approx 9 \text{ mm/s}$, close to the onset one finds $M \approx 300$. Indeed, as the onset Wi_c is approached from above M grows to infinity, and thus the criterion suggested in Ref. [23], $M \geq 1$, is not satisfied.

To summarize, we addressed in this paper five questions posed in the Introduction. First, we find that the strong prearranged perturbations are not necessary for elastic instabilities to occur in straight channel flows of visco-elastic fluid at $Re \ll 1$ and $Wi \gg 1$. Indeed, we observe the emergence of an elastic instability under smoothed and tapered inlet conditions at sufficiently high Wi , where the only possible source of weak but finite perturbation is a small cavity at the top channel wall used for pressure measurements. As a result, we find an elastic instability preceding three flow regimes, along with span-wise propagating elastic waves for $Wi > Wi_c$. This is the only coherent structure we found in the low-frequency range, on top of the continuous power spectra of the streamwise velocity and pressure fluctuations with power-law decays at higher frequencies. It should be emphasized that the dependence of the normalized velocity and pressure fluctuations on Wi , the emergence of the chaotic velocity and pressure spectra, and the non-linear dependence of the elastic wave frequency on Wi above the instability, exclude the Hopf bifurcation and its normal-mode nature as a possible explanation of the instability. Thus, the instability results from a non-normal mode bifurcation, similar to what was recently observed in a channel flow but with strong prearranged perturbations [15]. The elastic waves in Fig. 3 propagate in the span-wise direction, which is unlike the streamwise propagating elastic waves observed for strong perturbations at the inlet in Ref. [15]. Here, the elastic waves are prob-

ably too weak to energize a subsequent generation and synchronization of the CSs cycle. Finally, in contrast to previous observations of elastic waves [15, 22], here we were able to reveal their spatial and temporal structure downstream of the cavity. This allowed us to measure their frequency, wavelength, and propagation velocity v versus Wi based on space-time plots. Thus, the v dependence on Wi was measured, and their linear dispersion relation was confirmed directly for the first time.

We are grateful to Guy Han, Rostyslav Baron and Gershon Elazar for their assistance with preparing the experimental setup. This work was partially supported by the grants from the Israel Science Foundation (ISF; grant #882/15 and grant #784/19) and the Binational USA-Israel Foundation (BSF; grant #2016145). RS is grateful for the financial support provided by the Clore Israel Foundation.

[1] V. Steinberg, *Annu. Rev. Fluid Mech.* **53** (2021), [10.1146/annurev-fluid-010719-060129](https://doi.org/10.1146/annurev-fluid-010719-060129).

[2] R. G. Larson, *Rheol. Acta* **31**, 213 (1992).

[3] E. S. G. Shaqfeh, *Annu. Rev. Fluid Mech.* **28**, 129 (1996).

[4] P. Pakdel and G. H. McKinley, *Phys. Rev. Lett.* **77**, 2459 (1996).

[5] A. Groisman and V. Steinberg, *Nature* **405**, 53 (2000).

[6] A. N. Morozov and W. van Saarloos, *Phys. Rev. Lett.* **95**, 024501 (2005).

[7] N. Hoda, M. R. Jovanović, and S. Kumar, *J. Fluid Mech.* **601**, 407 (2008).

[8] M. R. Jovanović and S. Kumar, *J. Non-Newton. Fluid Mech.* **166**, 755 (2011).

[9] B. K. Lieu, M. R. Jovanović, and S. Kumar, *J. Fluid Mech.* **723**, 232 (2013).

[10] J. Page and T. A. Zaki, *J. Fluid Mech.* **742**, 520 (2014).

[11] D. Bonn, F. Ingremeau, Y. Amarouchene, and H. Kellay, *Phys. Rev. E* **84**, 045301 (2011).

[12] L. Pan, A. Morozov, C. Wagner, and P. E. Arratia, *Phys. Rev. Lett.* **110**, 174502 (2013).

[13] B. Qin and P. E. Arratia, *Phys. Rev. Fluids* **2**, 083302 (2017).

[14] B. Qin, P. F. Salipante, S. D. Hudson, and P. E. Arratia, *Phys. Rev. Lett.* **123**, 194501 (2019).

[15] N. K. Jha and V. Steinberg, ArXiv:2009.12258 (2020), submitted.

[16] P. G. Drazin and W. H. Reid, *Hydrodynamic stability*, 2nd ed. (Cambridge Univ. Press, London, 2004).

[17] P. J. Schmid, *Annu. Rev. Fluid Mech.* **39**, 129 (2007).

[18] F. Waleffe, *Physics of Fluids* **9**, 883 (1997), <https://doi.org/10.1063/1.869185>.

[19] N. K. Jha and V. Steinberg, ArXiv:2010.00426 (2020), submitted.

[20] Y. Liu, Y. Jun, and V. Steinberg, *Journal of Rheology* **53**, 1069 (2009).

[21] A. Liberzon, R. Gurka, Z. Taylor, D. Lasagna, M. Aubert, P. Bachant, C. Dallas, C. Curry, T. K aufer, A. Bauer, D. Bohringer, E. Zimmer, and P. Vennemann, “Openpiv-python,” (2014).

[22] A. Varshney and V. Steinberg, *Nat. Commun.* **10**, 652 (2019).

[23] D. D. Joseph, *Fluid dynamics of viscoelastic liquids* (Springer-Verlag Berlin Heidelberg GmbH, 1990).

[24] E. Balkovsky, A. Fouxon, and V. Lebedev, *Phys. Rev. Lett.* **84**, 4765 (2000).

[25] A. Fouxon and V. Lebedev, *Phys. Fluids* **15**, 2060 (2003).

[26] H. Alfvén, *Nature* **150**, 405 (1942).